Design and kinematic analysis of 3PSS-1S wrist for needle insertion guidance☆

Lisandro J. Puglisi*,[1], Roque J. Saltaren, Germán Rey Portolés[2], Hector Moreno, Pedro F. Cárdenas[3], Cecilia Garcia

Centro de Automática y Robótica, Universidad Politécnica de Madrid - CSIC, C. José Gutierrez de Abascal, 6. 28006, Madrid, Spain

ARTICLE INFO

Keywords:
Spherical wrist
Parallel manipulator
Needle insertion

ABSTRACT

In this work it is presented a complete kinematic analysis of the 3PSS-1S parallel mechanism for its implementation as a spherical wrist for a needle insertion guidance robot. The spherical 3PSS-1S mechanism is a low weight and reduced dimension parallel mechanism that allows spherical movements providing the requirements needed for the serial–parallel robotic arm for needle insertion guidance. The solution of its direct kinematic is computed with a numerical method based on the Newton–Raphson formulation and a constraint function of the mechanism. The input–output velocity equation is obtained with the use of screw theory. Three types of singular postures are identified during simulations and verified in the real prototype. The 3PSS-1S can perform pure rotations of ±45°, ±40°, ±60° along the $\boldsymbol{x}, \boldsymbol{y}, \boldsymbol{z}$ axes respectively.

1. Introduction

Contemporary medicine is toward less invasive and more localized therapy [1], mainly known as Minimally Invasive Surgery (MIS). One of this procedure is the percutaneous insertion of needles and catheters for biopsy, drug delivery and the placement of internal fiducials as surrogate for tumor location within the body.

Needle insertion intervention offers several advantages over traditional surgery, including less scarring, lighter anesthesia, reduced postoperative pain, reduced complications, and faster discharge from the hospital.

Currently, the conventional needle insertion procedure is a free-hand task with no exact reference for the entry point nor the direction of the needle. This is because the planing insertion process is based on the recognition of markers that the surgeon must place over the patient during the imagining session for further trajectory planning.

This methodology lacks accuracy and it is very common to make several erroneous insertions until the needle reaches the desired target, which may lead to internal hemorrhage and severe complications.

Robotic technologies can enhance the effectiveness of clinical procedures by coupling many information sources, such as volumetric medical images and perform complex actions in the operating room as reported in [2–6]. Particularly, a robotic device can insert needles with consistent accuracy and can overcome some of the shortcomings of the manual approach as mentioned in [7–12].

In this work we introduce the concept of a novel hybrid (serial–parallel) robotic arm for needle insertion guidance. The spherical parallel wrist is an improved version of the 3PSU-1S manipulator, whose dimensional synthesis was first reported in [13]. A discussion on the design and main attributes of the robot is presented. Then, the inverse and forward kinematics of the spherical wrist is stated, and a complete analysis of its singular configurations is detailed. Finally, the kinematic properties of the improved design are verified in the real enhanced spherical wrist prototype.

1.1. Needle insertion task requirements

During an insertion procedure, the surgical instrument must maintain a pre-planned path, defined by two points: the target point and the entry point. The first one, is where the tip of the instrument must reach, and the last one is where the needle is inserted into the patient (see Fig. 1(a)). The latter one is selected

☆ The authors would like to thank the financial support of the Spanish Government through the CICYT Project Ref. DPI2009-08778 and also to Comunidad de Madrid who supports the project ROBOCITY2030-II Ref. P2009/DPI-1559.

* Corresponding author. Tel.: +34 913 363 061.
E-mail addresses: lisandropuglisi@yahoo.com, lisandro.puglisi@alumnos.upm.es (L.J. Puglisi), rsaltaren@etsii.upm.es (R.J. Saltaren), grey@ruberinternacional.es (G. Rey Portolés), hmoreno@etsii.upm.es (H. Moreno), pfcardenash@unal.edu.co (P.F. Cárdenas), cecilia.garcia@upm.es (C. Garcia).

[1] Belongs to the MAEC-AECID grant programs.

[2] Hospital RUBER Internacional, Unidad de Radiofsica, Madrid, Spain.

[3] Professor Assistant from the Universidad Nacional de Colombia and grant COLCIENCIAS.

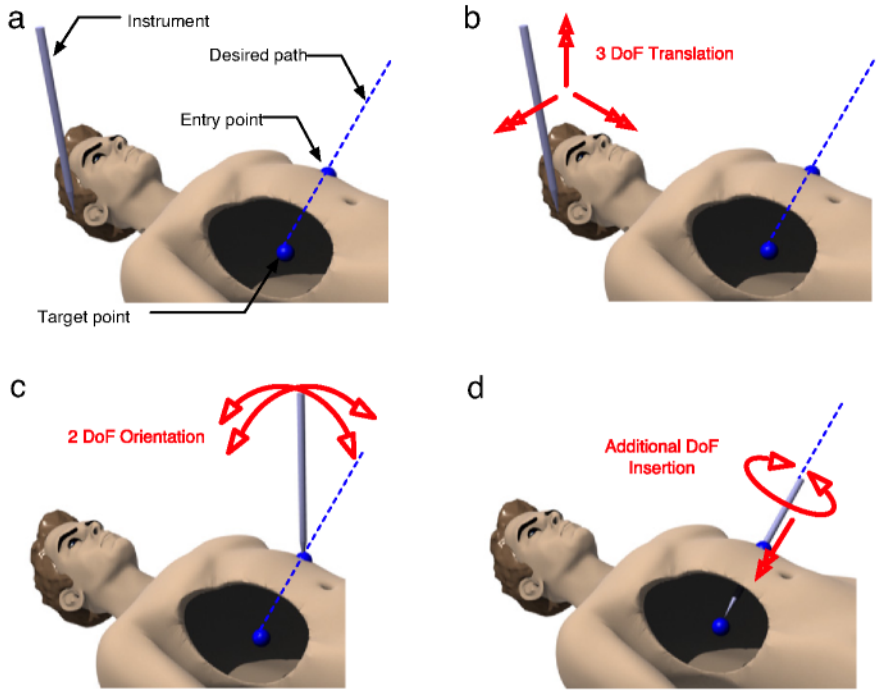

Fig. 1. Insertion procedure. 1(a): Trajectory definition. 1(b): Instrument's positioning. 1(c): Instrument's orientation. 1(d): Instrument's insertion.

in order that the desired path of insertion does not interfere with organs nor bones.

The insertion procedure can be summarized in the following steps. First, the tip of the needle must be placed at the entry point. This task requires 3 DoF (see Fig. 1(b)), then the needle must be aligned with the desired path, requiring at least 2 more DoF (see Fig. 1(c)). Once that the needle is correctly placed and aligned with the desired path at the entry point, the insertion procedure begins, generally with a twisting movement of the needle (see Fig. 1(d)).

Therefore, if the insertion is performed manually, a robotic device implemented as a guidance tool (i.e. it keeps the position and orientation) only requires 5 DoF.

However, if the insertion procedure is performed autonomously by the robot, it is preferable an additional DoF for the mechanism, since with 5 DoF only one reachable configuration is possible for each point of the desired path, resulting in a screw-like movement during insertion.

1.2. Overview of the mechanism

A robotic assistant must be carefully designed, in order to be accurate as well as rigid. Parallel mechanisms offer these physical properties, and some author have proposed them for the robotic needle insertion guidance [14–16]. However, the main drawback of a parallel mechanism is their reduced workspace. Although serial mechanisms overcome this problem [17], they present a real challenge in order to actuate the last DoFs of the mechanism without introducing backlash (due to the transmission system) or excessive load (direct transmission) at the end effector.

Therefore a better approach would be a design with a decoupled kinematic composed of a serial chain designed for the positioning and a low weight parallel wrist designed for orientation. The concept of this hybrid mechanism is presented in Fig. 2(a) (patent pending). As it was mentioned above, the mechanism consists of two main parts: the 3R serial arm and the spherical parallel wrist. The arm is mounted over a non-actuated sliding base that permits a gross positioning of the mechanism. A holding device supports the instrument at the end effector.

1.3. Design of the parallel spherical wrist

The principal criterion adopted for the design of the wrist mechanism is that, it will be coupled to the distal extremity of a serial arm. Thus, this mechanism must be compact, reduced size and light weight.

The general needle insertion procedure requires at least 5 DoF:3 DoF for the global positioning of the needle and 2 DoF for its correct orientation.

Even though an spherical wrist is redundant for the orientation task, this characteristic is preferable since it will allow different postures of the mechanism for a given trajectory. Furthermore, in an autonomous insertion, the extra DoFs will help to overcame problems related to tissue deformation during the insertion, by correcting the altered trajectory.

The design of a spherical parallel mechanism has been largely studied [18–20] and there exists many approaches for its synthesis [21–23]. However, given the ease of its implementation, a mechanism based on a passive spherical pair and three identical controlled spatial legs is applied in this study.

The 3PSS-1S is a four legs parallel mechanism, where the passive leg imposes the spherical movement pattern, controlled by three PSS type legs (prismatic–spherical–spherical chain) with the prismatic pair actuated. In a first approach [13] a PSU type leg was implemented but the universal pair had a reduced range of work, and tended to block the leg in several postures. Therefore, an extra degree of freedom was added to the kinematic chain, turning the leg into a PSS type (see Fig. 3).

2. Materials and methods

The kinematics of the 3PSS-1S is essentially the same of the 3PSU-1S (see [13]), since the extra revolute joint in each leg does not alter its kinematics. However, the inverse and instantaneous kinematic model of the SPM is presented again for clarity.

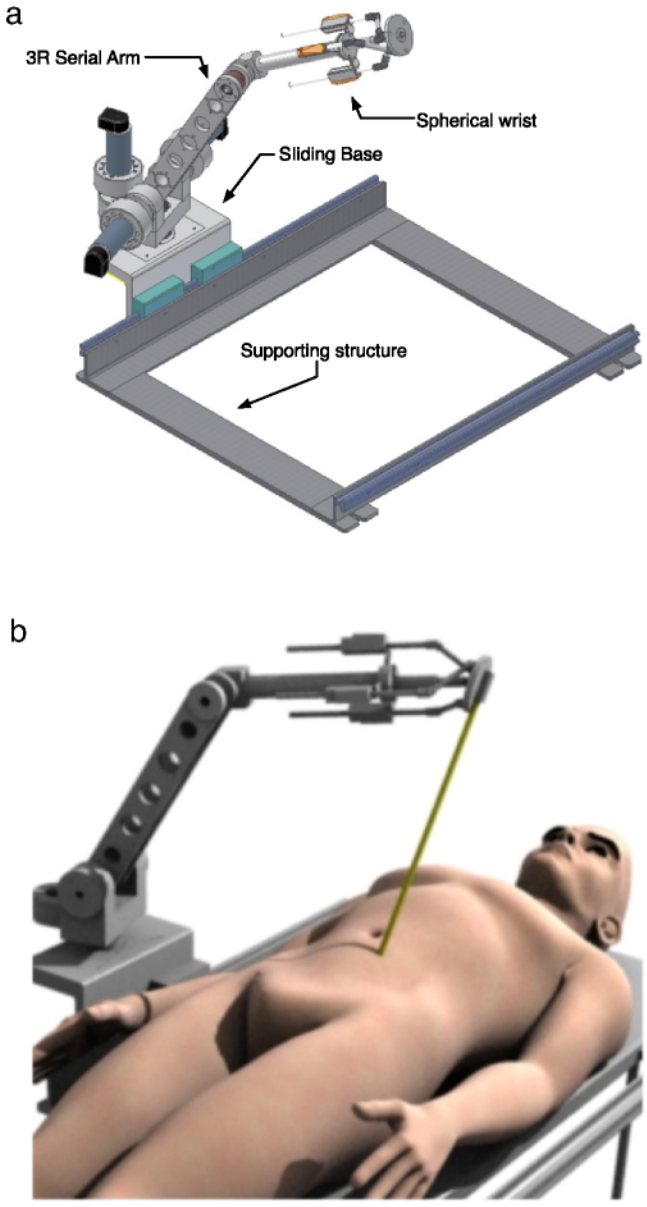

Fig. 2. Hybrid mechanism approach for robotic guided needle insertion. 2(a): Robotic arm concept. 2(b): Schematic robotic guided needle insertion.

Fig. 3. CAD of the 3PSS-1S spherical parallel wrist.

2.1. Inverse kinematics modeling

The inverse kinematic problem of the SPM, can be easily solved by considering:

1. The extreme of link L_7 (i.e. $B_i = [B_{i_x}, B_{i_y}, B_{i_z}]$) can only move over the surface of the sphere ζ_i with center in $C_i = [C_{i_x}, C_{i_y}, C_{i_z}]$ and radius L_7 (see Fig. 4(b)), given by (1):

$$(B_{i_x} - C_{i_x})^2 + (B_{i_y} - C_{i_y})^2 + (B_{i_z} - C_{i_z})^2 = {L_7}^2. \tag{1}$$

2. B_i corresponds with the distal extreme of the linear actuator, thus, B_i can only move over the line l_i defined by (2), whose direction vector $\hat{\boldsymbol{l}}_{\boldsymbol{i}} = [0, 0, 1]$ is associated to the axis of the prismatic actuator.

$$l_i : B_i = A_i + \lambda_i \hat{\boldsymbol{l}}_{\boldsymbol{i}}. \tag{2}$$

Equating (2) and (1), it can be demonstrated that $B_{i_x} = A_{i_x}$ and $B_{i_y} = A_{i_y}$. Taking this result into (1), B_{i_z} can be found according to (3)

$$B_{i_z} = C_{i_z} \pm \sqrt{{L_7}^2 - (A_{i_x} - C_{i_x})^2 - (A_{i_y} - C_{i_y})^2}. \tag{3}$$

Even though (3) has two possible solution $B_{i_z}^-, B_{i_z}^+$ whether choosing $-$ or $+$ sign in (3), only $B_{i_z}^-$ is considered, since the $B_{i_z}^+$ solution leads to collisions between the link L_7 and the moving platform. This can be seen in Fig. 4(b) where the distal extreme of L_7 (considering an ideal spherical joint with a full range of movement), points upwards for the $B_{i_z}^+$ solution, and as a consequence L_7 (dashed green line) will collide with the end effector.

Then, the state of the prismatic actuator is given by (4).

$$\lambda_i = B_{i_z} - A_{i_z}. \tag{4}$$

2.2. Direct kinematics modeling

As it is well known, finding the direct kinematic solution of a parallel mechanism is a complex task, and it is not always possible to find an analytic solution. In this work, the direct kinematic problem is solved by a numeric method based on the Newton–Raphson algorithm and a constraint function of the mechanism.

Lets consider the schematic diagram of the 3PSS-1S presented in Fig. 4, and lets define the constraint function for ith-leg of the mechanism given by Eq. (5).

$$f_i(\boldsymbol{p}) = \|\overrightarrow{OC_i} - (\overrightarrow{OA_i} + \overrightarrow{A_iB_i})\| - L_7 = 0 \tag{5}$$

where $\boldsymbol{p} = \begin{bmatrix} e_0, & e_1, & e_2, & e_3 \end{bmatrix}$ defines the orientation of the moving platform expressed in Euler parameters. $\overrightarrow{OC_i} = {}^{O}\boldsymbol{R}_P\, \tilde{\boldsymbol{c}}_i^T$, where ${}^{O}\boldsymbol{R}_P$ is the orientation of the end effector expressed as a rotation matrix, and $\tilde{\boldsymbol{c}}_{\boldsymbol{i}}$ is the skew antisymmetric matrix of $\boldsymbol{c}_i \cdot \overrightarrow{A_iB_i} = d_i \cdot \hat{\boldsymbol{z}}$ depends on the state of the ith-prismatic actuator.

The derivative of Eq. (5) with respect to the orientation of the end effector is given by Eq. (6).

$$\frac{d}{d\boldsymbol{p}}[f_i(\boldsymbol{p})] = f_{i_{\boldsymbol{p}}}(\boldsymbol{p}) = -2\hat{\boldsymbol{u}}_i\, {}^{O}\boldsymbol{R}_P\, \tilde{\boldsymbol{c}}_i\, \boldsymbol{G} \tag{6}$$

where $\hat{\boldsymbol{u}}_i$ is the unit vector of $\overrightarrow{B_iC_i}$, and $\boldsymbol{G}$ is the identity matrix of the Euler parameters given by Eq. (7), and satisfies $\boldsymbol{G}\,\boldsymbol{p}^T = 0$.

$$\boldsymbol{G} \equiv \begin{bmatrix} -e_1 & e_0 & e_3 & -e_2 \\ -e_2 & -e_3 & e_0 & e_1 \\ -e_3 & e_2 & -e_1 & e_0 \end{bmatrix}. \tag{7}$$

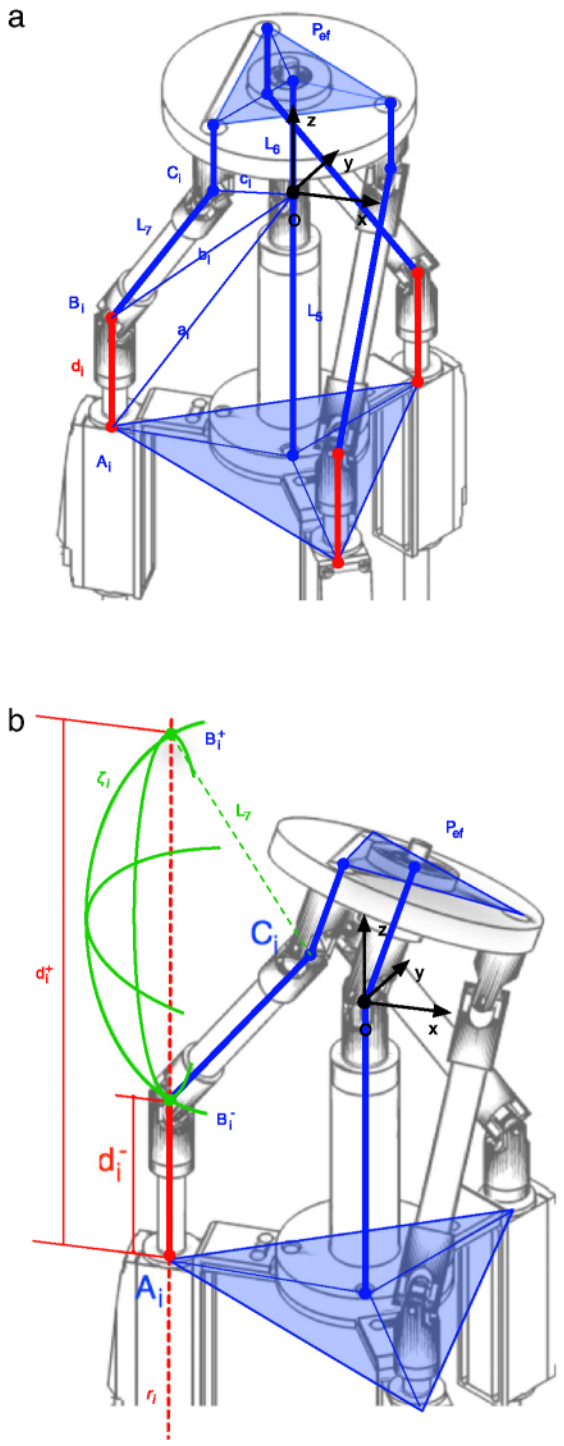

Fig. 4. Scheme of the 3PSS-1S. 4(a): Wire representation of the mechanism. The triangular shade defines the base and moving platforms. 4(b): Intersection of the spherical characteristic of link L_7 and linear motion of point B_i.

Arranging the constraint functions for legs $i = 1, 2, 3$ into matrix form the constraint vector of the mechanism is found.

$$\boldsymbol{\Phi}(\boldsymbol{p}) = \begin{bmatrix} f_1(\boldsymbol{p}) \\ f_2(\boldsymbol{p}) \\ f_3(\boldsymbol{p}) \end{bmatrix} = \mathbf{0}. \tag{8}$$

Taking the derivative of the constraint vector of the mechanism with respect to the orientation of the end effector, a Jacobian matrix can be defined as,

$$\boldsymbol{\Phi}_{\boldsymbol{p}}(\boldsymbol{p}) = \begin{bmatrix} f_{1\boldsymbol{p}} \\ f_{2\boldsymbol{p}} \\ f_{3\boldsymbol{p}} \end{bmatrix} = \begin{bmatrix} -2\hat{\boldsymbol{u}}_1\, {}^{O}\boldsymbol{R}_P\, \tilde{\boldsymbol{c}}_1\, \boldsymbol{G} \\ -2\hat{\boldsymbol{u}}_2\, {}^{O}\boldsymbol{R}_P\, \tilde{\boldsymbol{c}}_2\, \boldsymbol{G} \\ -2\hat{\boldsymbol{u}}_3\, {}^{O}\boldsymbol{R}_P\, \tilde{\boldsymbol{c}}_3\, \boldsymbol{G} \end{bmatrix}. \tag{9}$$

The Newton–Raphson algorithm makes possible to find a solution to Eq. (8), iterating Eq. (10) from an initial estimate $\boldsymbol{p}_0$, until $\|\Phi(\boldsymbol{p})\| < \epsilon$ is satisfied.

$$\boldsymbol{p}^{(k+1)} = \boldsymbol{p}^{(k)} + \boldsymbol{\Phi}_{\boldsymbol{p}}^{(k)^{-1}} \cdot \boldsymbol{\Phi}^{(k)} \tag{10}$$

where $k = 0, 1, \ldots$ is the iteration cycle, and ϵ is the defined error tolerance. Since $\boldsymbol{\Phi}_{\boldsymbol{p}}$ is not square the Moore–Penrose pseudoinverse is implemented in order to obtain $\boldsymbol{\Phi}_{\boldsymbol{p}}^{-1}$.

This method is highly dependent of the initial estimation ($\boldsymbol{p}^{(0)}$), thus the method may diverge if poor initial estimation is given. Another consideration that must be taken is that the numerical method depends on the evaluation of $\boldsymbol{\Phi}_{\boldsymbol{p}}^{(k)}$, and that it may not converge if a $\boldsymbol{\Phi}_{\boldsymbol{p}}^{(k)} = \mathbf{0}$ condition is met. Therefore for the computational implementation of the algorithm, a maximum of 100 iterations is established in order to prevent infinite iterations. If the method does not find a solution in 100 iterations it is assumed that the method diverge.

2.3. Instantaneous kinematics

The input–output velocity equation the SPM is found applying the screw theory formulation. This methodology provides a better geometrical insight into the problem and facilitate the analysis of singularities [24], even more, it avoids the tedious and prone to error problem of differentiating the kinematic model.

Therefore, defining an instantaneous reference frame $O'_{x'y'z'}$, which is instantaneously coincident and parallel to the reference frame O_{xyz} and expressing all the twists of the mechanism with respect to this instantaneous reference frame (see Fig. 5), the resulting instantaneous movement (twist) of the end effector ($\$_{ef}$), can be found as follows [25]:

$$\begin{aligned} \$_{ef} &= \begin{bmatrix} \boldsymbol{\omega}_{ef} \\ \boldsymbol{v}_{O'} \end{bmatrix} \\ &= \dot{q}_{1,i}\,\hat{\$}_{1,i} + \dot{q}_{2,i}\,\hat{\$}_{2,i} + \dot{q}_{3,i}\,\hat{\$}_{3,i} + \dot{q}_{4,i}\,\hat{\$}_{4,i} + \cdots + \dot{q}_{5,i}\,\hat{\$}_{5,i} \\ &\quad + \dot{q}_{6,i}\,\hat{\$}_{6,i} + \dot{q}_{7,i}\,\hat{\$}_{7,i} \end{aligned} \tag{11}$$

where $\boldsymbol{\omega}_{ef} = \begin{bmatrix} \omega_x, & \omega_y, & \omega_z \end{bmatrix}^T$, is the angular velocity of the end effector, $\boldsymbol{v}_{O'} = \begin{bmatrix} v_{Ox'}, & v_{Oy'}, & v_{Oz'} \end{bmatrix}^T$ is the linear velocity of a point that belongs to the end effector expressed at the origin of the instantaneous reference frame, $\hat{\$}_{j,i}$ is the unitary twist associated to the jth-joint of the ith-leg, and $\dot{q}_{j,i}$ is its corresponding intensity.

The spherical pattern of movement of the mechanism is governed by the spherical joint of the passive leg therefore, translations are not possible, i.e. $\boldsymbol{v}_{O'} = \begin{bmatrix} 0, & 0, & 0 \end{bmatrix}^T$.

Defining a reciprocal screw $\$_0$ that passes through the center of both spherical joints for each leg, given by (12),

$$\hat{\$}_{r,i} = \begin{bmatrix} \boldsymbol{u}_{r,i} \\ \boldsymbol{b}_i \times \boldsymbol{u}_{r,i} \end{bmatrix}, \tag{12}$$

where $\boldsymbol{u}_{r,i} = (\boldsymbol{c}_i - \boldsymbol{b}_i)/\|\boldsymbol{c}_i - \boldsymbol{b}_i\|$, and applying the reciprocal product to the linear combination of the twists of each leg, (11) is reduced to:

$$[\boldsymbol{\Pi}\,\hat{\$}_{r,i}]^T\,\hat{\$}_{ef} = \dot{q}_{1,i}\,([\boldsymbol{\Pi}\,\hat{\$}_{r,i}]^T\,\hat{\$}_{1,i}) \tag{13}$$

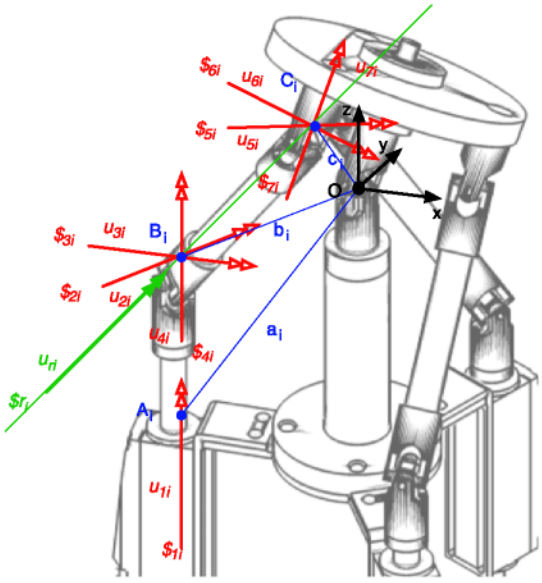

Fig. 5. Screws associated to the 3PSS-1S parallel mechanism.

where $\hat{\$}_{1,i} = \begin{bmatrix}\mathbf{0}, & \boldsymbol{u}_{1,i}\end{bmatrix}^T$ is the twist $\$_\infty$ associated to the prismatic joint, and the reciprocal product operator $\boldsymbol{\Pi}$ is defined as follows:

$$\boldsymbol{\Pi} = \begin{bmatrix} \boldsymbol{\emptyset} & \boldsymbol{I} \\ \boldsymbol{I} & \boldsymbol{\emptyset} \end{bmatrix} \tag{14}$$

where $\boldsymbol{I}$ is the 3×3 identity matrix and $\boldsymbol{\emptyset}$ is the 3×3 zero matrix [21].

Replacing $\hat{\$}_{1,i}$ and $\$_{ef}$ in (13), and expanding for legs $i = 1, 2, 3$, the velocity equation of the mechanism can be found according to (15).

$$\begin{bmatrix} (\boldsymbol{b}_1 \times \boldsymbol{u}_{r,1})^T \\ (\boldsymbol{b}_2 \times \boldsymbol{u}_{r,2})^T \\ (\boldsymbol{b}_3 \times \boldsymbol{u}_{r,3})^T \end{bmatrix} \boldsymbol{\omega}_{ef} = \begin{bmatrix} \boldsymbol{u}_{r,1}^T \boldsymbol{u}_{1,1} & 0 & 0 \\ 0 & \boldsymbol{u}_{r,2}^T \boldsymbol{u}_{1,2} & 0 \\ 0 & 0 & \boldsymbol{u}_{r,3}^T \boldsymbol{u}_{1,3} \end{bmatrix} \times \begin{bmatrix} \dot{q}_{1,1} \\ \dot{q}_{1,2} \\ \dot{q}_{1,3} \end{bmatrix}. \tag{15}$$

Defining $\boldsymbol{J_x}$ and $\boldsymbol{J_q}$ as Eqs. (17) and (18), respectively, the velocity equation of the mechanism can be expressed as:

$$\boldsymbol{J_x}\, \boldsymbol{\omega}_{ef} = \boldsymbol{J_q}\, \dot{\boldsymbol{q}} \tag{16}$$

where $\dot{\boldsymbol{q}} = \begin{bmatrix} q_{1,1}, & q_{1,2}, & q_{1,3} \end{bmatrix}^T$ and

$$\boldsymbol{J_x} = \begin{bmatrix} (\boldsymbol{b}_1 \times \boldsymbol{u}_{r,1})^T \\ (\boldsymbol{b}_2 \times \boldsymbol{u}_{r,2})^T \\ (\boldsymbol{b}_3 \times \boldsymbol{u}_{r,3})^T \end{bmatrix} \tag{17}$$

$$\boldsymbol{J_q} = \begin{bmatrix} \boldsymbol{u}_{r,1}^T \boldsymbol{u}_{1,1} & 0 & 0 \\ 0 & \boldsymbol{u}_{r,2}^T \boldsymbol{u}_{1,2} & 0 \\ 0 & 0 & \boldsymbol{u}_{r,3}^T \boldsymbol{u}_{1,3} \end{bmatrix}. \tag{18}$$

If the inverse matrix of $\boldsymbol{J_q}$ exists, the velocity equation of the mechanism can be written in terms of the overall Jacobian matrix $\boldsymbol{J} = \boldsymbol{J_q}^{-1} \boldsymbol{J_x}$, as follows:

$$\boldsymbol{J}\, \boldsymbol{\omega}_{ef} = \dot{\boldsymbol{q}}. \tag{19}$$

2.4. Singular configurations

The 3PSS-1S has three identified posture where the input–output velocity equation cannot be solved (singular configuration), therefore the mechanism looses its capability of being controlled (see Fig. 6).

The first identified singular configuration (Type I) corresponds when the twist of the prismatic joint and the reciprocal screw of the same leg are perpendicular (see Fig. 6(a)). In this configuration the twist and the reciprocal screw becomes reciprocal to each other, thus the orthogonal product $\$_{r,1} \circ \$_{1,i}$ becomes zero, and a complete column of $\boldsymbol{J_q}$ will be zero as well. As a consequence there would be no transmission from the actuation to the end effector, and the moving platform will lose one degree of freedom. This configuration can be defined as an inverse kinematic singularity.

The second identified singular configuration (Type II) is a particular case of the previous one, and corresponds when the three legs have their links perpendicular. As a consequence, the moving platform is completely blocked. (See Fig. 6(b).)

The third identified singular configuration (Type III) occurs when the lines associated to each reciprocal screws intersect at a common point, that we shall name $P_\cap$ (see Fig. 6(c)). This particular point belongs to the screw axis of the three reciprocal screw, and $\boldsymbol{J_x}$ can be redefined as Eq. (20).

$$\boldsymbol{J_x} = \begin{bmatrix} ({}^O p_\cap \times \boldsymbol{u}_{r,1})^T \\ ({}^O p_\cap \times \boldsymbol{u}_{r,2})^T \\ ({}^O p_\cap \times \boldsymbol{u}_{r,3})^T \end{bmatrix} \tag{20}$$

where ${}^O p_\cap$ is the direction vector from the global reference frame O_{xyz} to the intersection point $P_\cap$.

Therefore, each row of $\boldsymbol{J_x}$ will be perpendicular to ${}^O p_\cap$, and they will belong to a plane whose normal vector is ${}^O p_\cap$. Since these vector are coplanar, then, one of them is linearly dependent of the other two. Thus, $\boldsymbol{J_x}$ loses its rank, and becomes singular. In this posture the mechanism cannot withstand any external couple in the $\boldsymbol{w}$ direction. It can be said that the mechanism is in a direct kinematic singular configuration.

2.5. Simulation methodology

2.5.1. Workspace generation

The procedure performed to calculate and obtain the workspace is based on a numerical method that generates all the orientations of the 3D space, and verifies that the mechanism does not exceed its physical limitations. These limitations are given by the implicit constraints of the kinematics chains described below:

1. Prismatic Stroke Constraint: the prismatic stroke constraint imposed on each leg can be written as $d_{min} \leq d_i \leq d_{max}$. Where d_i is the state of the prismatic joint of the ith-limb given by Eq. (4), and d_{min} and d_{max} are the minimum and maximum stroke of the actuator.
2. Spherical Joint Constraint: it is considered that its relative movement can never exceed the region limited by the circular cone defined by an axis normal to the joint, an aperture angle δ_{max} and its apex located at the center of the spherical joint [26].
3. Leg Interference: it is based on the evaluation of the minimum distance between two cylinders [27]. In this work, it is only considered the interference between links L_{7_i} and link L_5, because the constraints imposed by the spherical joints do not allow collisions between other elements.

In this study, the quaternion representation method for the orientation is used [28]. This method provides a solid sphere

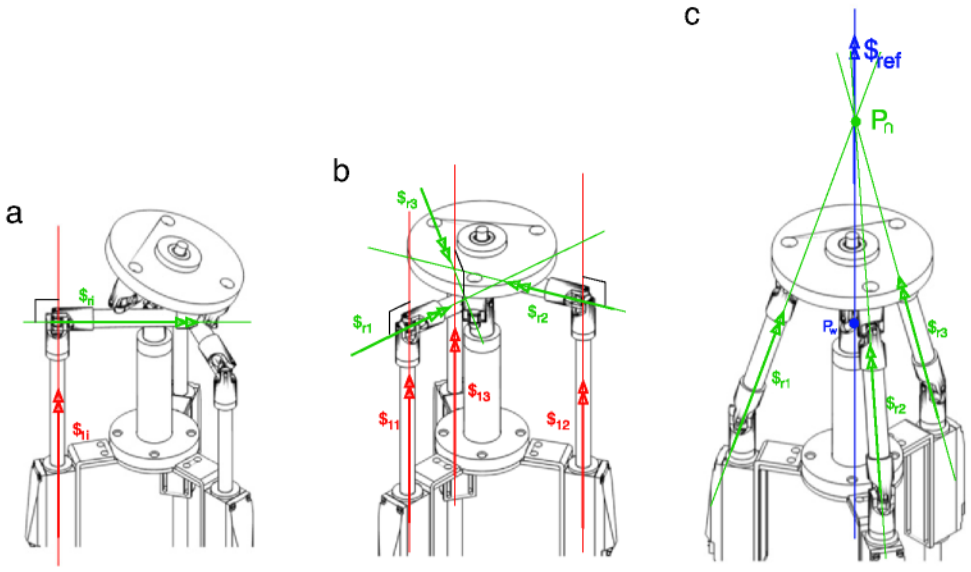

Fig. 6. Singular configurations. 6(a): Type I, single leg blocked. 6(b): Type II, all legs blocked. 6(c): Type III, screws axis intersection.

representation for all the orientation of the 3D space. A point of the solid sphere defines a vector $\boldsymbol{x} = \begin{bmatrix} e_1, & e_2, & e_3 \end{bmatrix} = \begin{bmatrix} \hat{\boldsymbol{k}} \sin(\theta/2) \end{bmatrix}$, where its direction is associated to the rotation axis ($\hat{\boldsymbol{k}} = \pm \boldsymbol{x}/\|\boldsymbol{x}\|$) and its norm is related with the angle of rotation according to $\theta = \pm 2 \arcsin(\|\boldsymbol{x}\|)$. The $\pm$ sign depends whether $e_3 \geq 0$ or $e_3 < 0$, respectively. The z-coordinate of the direction vector $\hat{\boldsymbol{k}} = \begin{bmatrix} k_x, & k_y, & k_z \end{bmatrix}$ is considered always $k_z \geqslant 0$ in order to avoid ambiguities on the orientation representation.

2.5.2. Singularity analysis

A singular configuration occurs when the instantaneous kinematics of the mechanism $\boldsymbol{J_x}\,\boldsymbol{\omega}_{ef} = \boldsymbol{J_q}\,\dot{\boldsymbol{q}}$ becomes indeterminate, i.e. when $\boldsymbol{J_x}$ or $\boldsymbol{J_q}$ or both matrices are singular, thus the velocity equation cannot be solved.

Therefore, the singularity analysis procedure can be focused to find when these matrices become singular.

A numerical approach, can be based on the evaluation of the determinant of the Jacobian matrix ($\boldsymbol{J} = \boldsymbol{J_q}^{-1}\boldsymbol{J_x}$), and to find when it becomes zero or very close to it. In practice, sometimes it is not easy to find configurations with this special characteristic, and another criteria must be adopted. For this reason, in this work, the change of sign of the determinant is considered instead, and it is evaluated during the workspace generation.

2.5.3. Dexterity analysis

The performance of a robot in terms of force and velocity transmission can be quantified with the condition index of the Jacobian matrix [29], given by (21).

$$CI(J) = \frac{1}{\kappa(\boldsymbol{J})} \tag{21}$$

where $\kappa(\boldsymbol{J}) = |\boldsymbol{J}| \cdot |\boldsymbol{J}^{-1}|$ is the condition number of the Jacobian matrix. Expression (21) can only take values between $0 < CI(\boldsymbol{J}) \leq 1$. When CI approaches to zero, the Jacobian Matrix is bad conditioned, and the mechanism is near to a singular configuration. This index give us a local idea of the configuration of the mechanism. In order to get a global idea of the performance of the mechanism, the Global Condition Index is introduced as follows, where W represents the workspace, and it can only takes values in the interval $(0,\ 1]$.

$$GCI = \frac{\int_W CI(\boldsymbol{J})dW}{\int_W dW}. \tag{22}$$

Table 1
3PSS-1S geometry.

Element	Parameter	Dimensions
Moving platform	Radius	24 mm
Fixed platforms	Radius	50 mm
Fixed leg (L_5)	Radius	7.5 mm
	Length	100 mm
Link L_6	Radius	7.5 mm
	Length	28 mm
Moving leg (L_7)	Radius	5 mm
	Length	65 mm
Spherical joint	δ_{max}	90°
Linear actuator	$d_{1_{min}}$	15 mm
	$d_{1_{max}}$	155 mm

3. Results

The geometric characteristics of the mechanism considered for the simulations are summed up in Table 1. Some of these dimensions differ from [13], due to the mechanical improvements introduced in this prototype.

3.1. Workspace analysis

The workspace generation algorithm was implemented in Matlab®, and more than 4.2 millions of possible orientation for the end effector were generated and evaluated.

From the 4.2 millions of orientations evaluated, only 927 064 passed the constraints verification procedure and its graphical representation is presented in Fig. 7.

Considering that a point of the sphere is given by $\boldsymbol{x} = [e_1,\ e_2,\ e_3] = [\hat{\boldsymbol{k}} \sin(\theta/2)]$, where $\hat{\boldsymbol{k}}$ is an unit vector associated with the rotation axis, the maximum pure rotation of the mechanism can be found by slicing the solid representation of the workspace with planes $e_3 = 0$ and $e_1 = 0$ as shown in Fig. 8.

The pure rotations characteristics of the mechanism are summed up in Table 2, where ψ, θ and ϕ corresponds to quantity rotated over the $\boldsymbol{x}$, $\boldsymbol{y}$ and $\boldsymbol{z}$ axis of the reference frame O_{xyz}.

3.2. Singularity analysis

In Fig. 9, the volumetric representation of those configurations where the sign of the determinant of the Jacobian matrix is

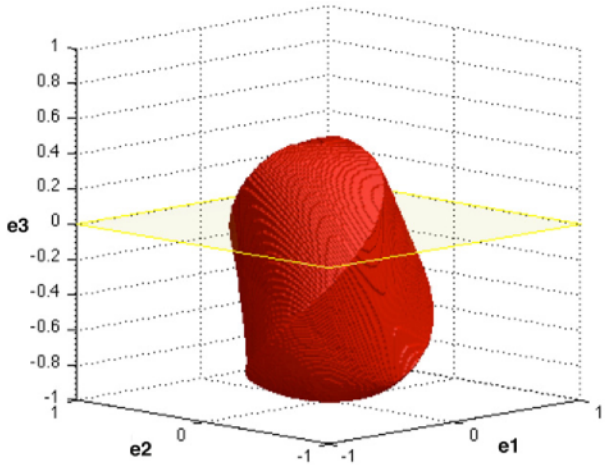

Fig. 7. Volumetric representation of the workspace of the 3PSS-1S.

Table 2
3PSS-1S pure rotations characteristics.

Parameter	Quaternion	Angle
$e_{1_{\min}} = -0.421$	[0.9071, −0.4210, 0, 0]	$\psi_{\min} = -49.8°$
$e_{1_{\max}} = 0.531$	[0.8474, 0.5310, 0, 0]	$\psi_{\max} = 64.1°$
$e_{2_{\min}} = -0.481$	[0.8767, 0, −0.481, 0]	$\theta_{\min} = -57.5°$
$e_{2_{\max}} = 0.441$	[0.8975, 0, 0.441, 0]	$\theta_{\max} = 52.3°$
$e_{3_{\min}} = -1$	[0, 0, 0, −1]	$\phi_{\min} = -180°$
$e_{3_{\max}} = 0.486$	[0.8740, 0, 0, 0.4860]	$\phi_{\max} = 58.1°$

negative (represented as a yellow volume) is superposed over the solid representation of the workspace. The boundary of this new volume defines a surface that separates the space into the regions where the determinant has positive sign and negative sign. Hence, this surface also defines the configurations where the determinant of the Jacobian matrix is zero.

As it can be seen in Fig. 9, the singular surface intersects the workspace, which implies that the mechanism poses singular configurations inside its workspace.

This intersection can be analyzed in detail by slicing the solid representation of the workspace and the determinant with different planes e_1 as shown in Fig. 10. From these slices, it can be observed that the singular surface divides the workspace into two regions, thus reducing the effective workspace of the mechanism.

In fact, considering the slice $e_1 = 0$, presented in Fig. 10(b), the minimum pure rotation free of singularities over the $\boldsymbol{w}$ axis of the sphere is now $\phi_{\min} = -60°$ defined by $e_{3_{\min}} = -0.5$ approximately.

The portion of the singular surface that divides the workspace, corresponds to the postures where the mechanism presents a Type III singular configuration (6(c)).

In Fig. 10(b), it can be seen that the solid representation of the workspace and the singular surface intersects at $\boldsymbol{p} = [0, 0, 0, -1]$. For this orientation, the mechanism presents a Type II singular configuration, as shown in Fig. 6(b).

3.3. Dexterity analysis

During the 3PSS-1S volumetric workspace generation, the condition index of the Jacobian matrix was also evaluated, and it is presented in Fig. 10 as 2D maps over the slices of workspace of the mechanism and the determinant of the Jacobian matrix.

As it can be seen from the dexterity map representations, the Jacobian matrix presents a good conditioning for the top and bottom region of the workspace, and it decreases while getting closer to the singular surface given by the determinant of the Jacobian matrix.

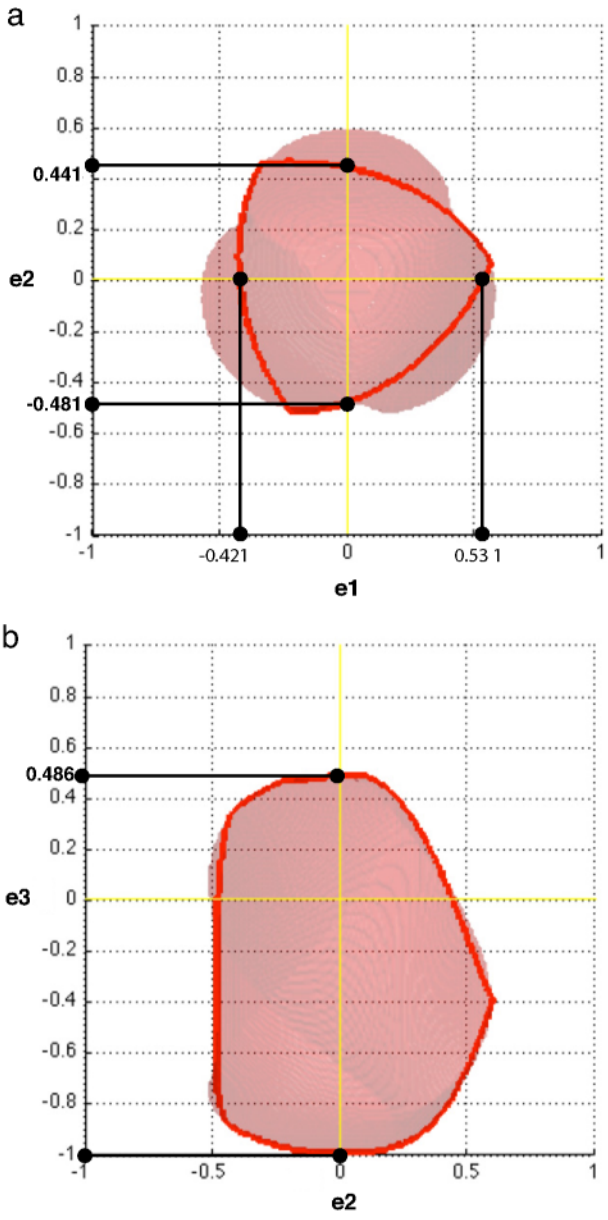

Fig. 8. Maximum pure rotation. The red closed curve defines the boundaries of the workspace at the specified slice. 8(a): Slice for $e_3 = 0$. 8(b): Slice for $e_1 = 0$. (For interpretation of the references to colour in this figure legend, the reader is referred to the web version of this article.)

It can be also seen, that the dexterity map shows an abrupt change near the top region of the workspace. This change in the map, reveals the possible existence of singular configurations that could not be detected via the determinant analysis.

Taking a closer look at the dexterity map presented in Fig. 10(e), it is observed that this change occurs at $\boldsymbol{p} = [0.8752, 0, 0, 0.4838]$. This orientation of the moving platform corresponds when the base and the moving platform are parallel but rotated 58° over the $\boldsymbol{w}$ axis of the spherical joint of the passive leg, which corresponds to a Type II singular configuration (Fig. 6(b)). Therefore, Type II singularities appears at extreme rotation over the $\hat{\boldsymbol{z}}$ axis.

The global condition index found is $GCI = 0.1743$.

3.4. Experimental testbed of the 3PSS-1S

The modification previously mentioned are implemented in the former 3PUS-1S prototype. The dimensions of the improved

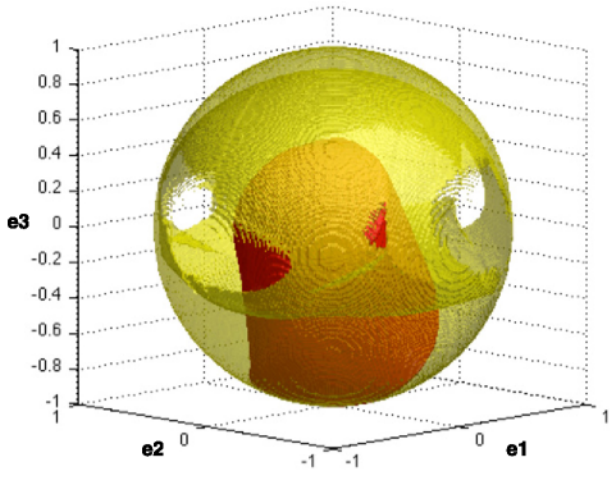

Fig. 9. Volumetric representation of determinant (yellow) superposed over the volumetric representation of the workspace (red). (For interpretation of the references to colour in this figure legend, the reader is referred to the web version of this article.)

prototype does not differs much from the previous one, it weights less than 500 g, and it fits inside a circular cylinder of 70 mm of radius and 150 mm of longitude.

The 3PSS-1S spherical wrist uses 3 Faulhaber Linear DC-Servomotors LM 1247 080-01 for actuation in combination with the MCLM 3003/06 S drive electronics. These linear motor are composed of a magnetized rod that slides inside a controlled magnetic field, providing a controlled linear motion that can freely rotate over its axis of action. Given the reduced range of work of the spherical joint commercially available, they were replaced by an universal joint and a revolute joint orthogonally placed (see Fig. 11). The parts of the spherical wrist are machined on aluminum, and white ABS (Acrylonitrile butadiene styrene).

Table 3
Comparison table of the 3PSS-1S rotations characteristics.

Parameter	Real prototype	Simulation results
ψ_{min}	−45°	−49.8°
ψ_{max}	45°	64.1°
θ_{min}	−40°	−57.5°
θ_{max}	40°	52.3°
ϕ_{min}	−60°	−60°
ϕ_{max}	60°	58.1°

The control architecture of the experimental testbed is presented in Fig. 12. The kinematic model of the parallel spherical wrist detailed in Section 2 is implemented in Labview, and via a CAN bus the linear motors are commanded.

The results obtained during simulation are validated in the real prototype, with a IMU placed over the end effector. The singular configuration of the real mechanism are presented in Fig. 13. A comparison between the results obtained from simulations and with the real prototype are presented in Table 3. In must be remarked that the IMU (i.e. 9 DOF razor IMU v14) used was susceptible to the magnet fields generated by the linear actuator, therefore the data had to be filtered and rounded to the near integer. Even though the resolution of the sensor is low (i.e. 1°) after this processing, it is more than enough for our evaluation purposes.

As it can be observed there exist discrepancies between the simulation results and the experimental data. In particular, the maximum rotation of the real prototype over the $\hat{\boldsymbol{x}}$ and $\hat{\boldsymbol{y}}$ axes are clearly smaller than those obtained during simulation. This variability is caused by the real range of work of spherical joint of the passive leg, since the spherical joints are obtained from the coupling of a universal joint and a revolute joint.

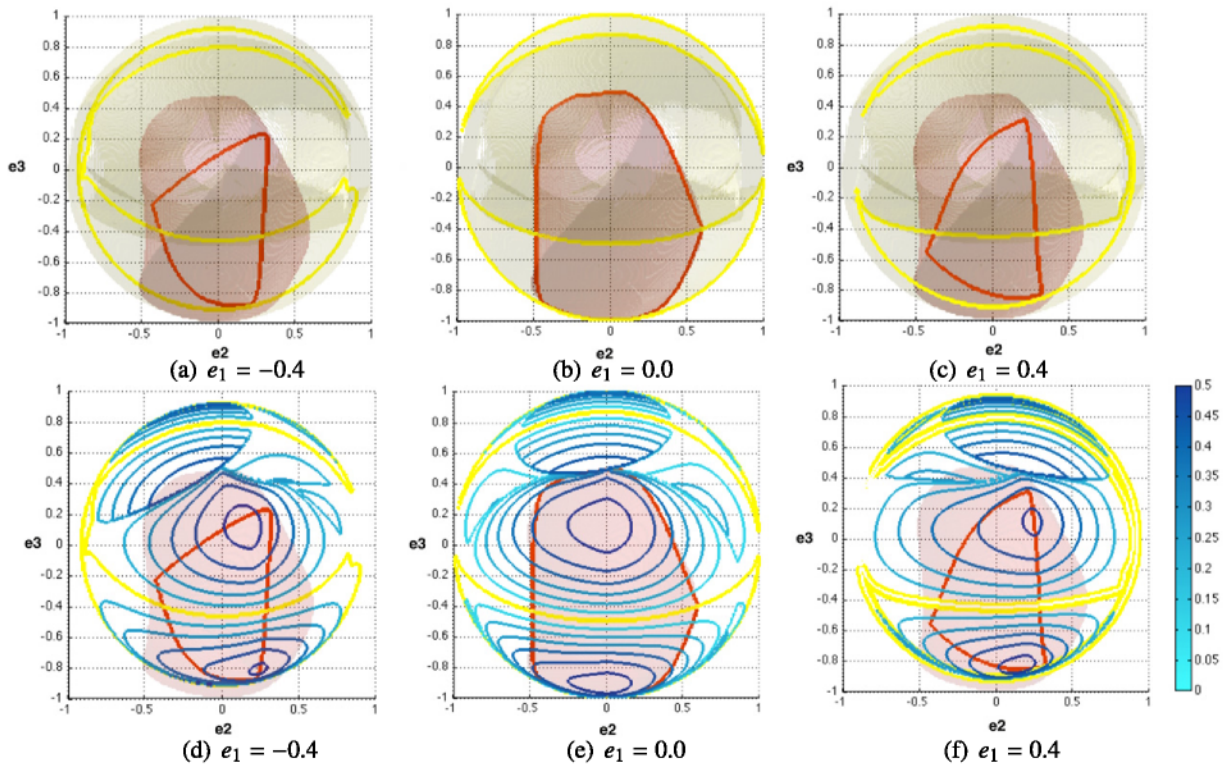

Fig. 10. Singularities and dexterities of the spherical parallel wrist. Slices of the volumetric representations. The red contour defines the boundaries of the workspace, and the yellow contour defines the boundaries of the sign of the determinant. Slices of the volumetric representations with the 2D map for the CI. The blue scaled contour represents the CI. (For interpretation of the references to colour in this figure legend, the reader is referred to the web version of this article.)

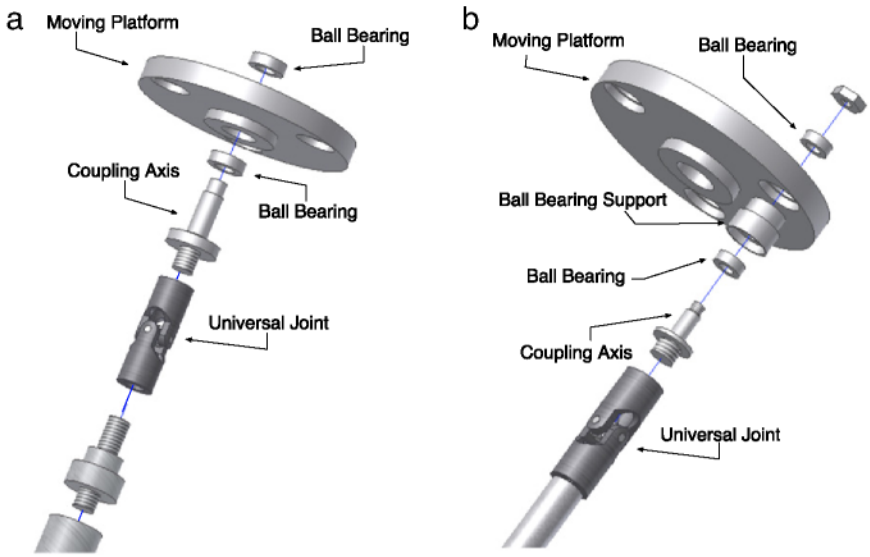

Fig. 11. Details of the adaptation of the universal joints connected to the moving platform of the passive leg (11(a)) and of the active leg (11(b)).

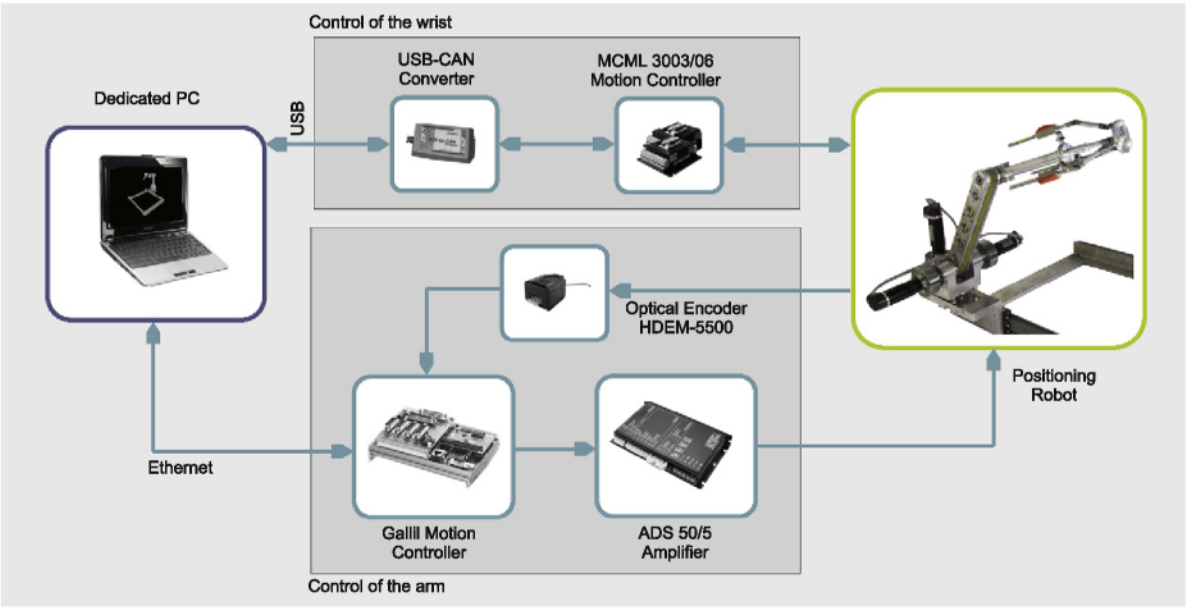

Fig. 12. Robotic arm architecture.

4. Conclusions and discussion

A spherical wrist prototype for a robotic needle insertion guidance based on a spherical parallel mechanism 3PSS-1S has been developed.

The 3PSS-1S spherical mechanism is a low weight and reduced dimension parallel mechanism that allows spherical movements, with similar characteristic obtained during simulation. However, the real prototype presents a less range of rotation over the $\hat{\boldsymbol{x}}$ and $\hat{\boldsymbol{y}}$ axes, than the obtained during simulation. This discrepancy between simulation and experimental results are principally caused by the non ideal characteristics of the spherical pair of the passive leg, which was implemented as a universal joint plus a revolute joint.

The mechanism poses three singular posture within its workspace, where it blocks or loses one or more degrees of freedom, reducing its effective workspace. Since these singular postures are located on the boundaries of the effective workspace, they can be avoided by programmatically restricting the stroke of the actuator.

The solution proposed for the direct kinematic problem is a numerical method based on the Newton–Raphson algorithm and a constraint function of the mechanism. In spite the fact that the numerical method is dependent of the initial estimate, it has shown robustness for all the orientations that belongs to the workspace of the mechanism.

The solid representation of the workspace based on the representation of the elements of the unit quaternion, provides a simple tool for the analysis of the main characteristics of an orientation mechanism. The maximum pure rotation can be easily obtained by analyzing the workspace at the principal planes.

The singularity and dexterity analysis of the mechanism based on the analysis of the determinant and the condition index of the Jacobian matrix corresponds with the singular posture identified of the mechanism. Therefore, the numerical analysis proposed can be used as a first approach for the determination of the singular

(a) Home. (b) Type I. (c) $\phi_{min} = -60°$. Type III. (d) $\phi_{max} = 60°$. Type II.

Fig. 13. 3PSS-1S real prototype.

configurations of the mechanism. Even tough, a serious singularity analysis must always consider a deep analysis of the input–output velocity equation.

The overall mechanism proposed for the needle insertion guidance is a 6 DOF mechanism, resulting in a redundant mechanism for the needle insertion guidance, which requires only 5 DOF. Therefore, this extra DOF for the task allows to overcome the limitation of the wrist due to its physical constraints and singularities postures.

References

[1] M. Vierra, Minimally invasive surgery, Annual Review of Medicine (1995) 147–158. http://dx.doi.org/10.1146/annurev.med.46.1.147.

[2] P. Kazanzides, G. Fichtinger, G. Hager, A. Okamura, L. Whitcomb, R. Taylor, Surgical and interventional robotics—core concepts, technology, and design, IEEE Robotics & Automation Magazine (2) (2008) 122–130. http://dx.doi.org/10.1109/MRA.2008.926390.

[3] G. Fichtinger, P. Kazanzides, A.M. Okamura, G.D. Hager, L.L. Whitcomb, R.H. Taylor, Surgical and interventional robotics: part II: surgical CAD–CAM systems, IEEE Robotics & Automation Magazine/IEEE Robotics & Automation Society (3) (2008) 94–102. http://dx.doi.org/10.1109/MRA.2008.927971.

[4] G.D. Hager, A.M. Okamura, P. Kazanzides, L.L. Whitcomb, G. Fichtinger, R.H. Taylor, Surgical and interventional robotics: part III: surgical assistance systems, IEEE Robotics & Automation Magazine/IEEE Robotics & Automation Society (4) (2008) 84–93. http://dx.doi.org/10.1109/MRA.2008.930401.

[5] D.B. Camarillo, T.M. Krummel, J.K. Salisbury, Robotic technology in surgery: past, present, and future, American Journal of Surgery (4A Suppl.) (2004) 2S–15S. http://dx.doi.org/10.1016/j.amjsurg.2004.08.025.

[6] J.S. Navarro, N. Garcia, C. Perez, E. Fernandez, R. Saltaren, M. Almonacid, Kinematics of a robotic 3UPS1S spherical wrist designed for laparoscopic applications, The International Journal of Medical Robotics + Computer Assisted Surgery: MRCAS (3) (2010) 291–300. http://dx.doi.org/10.1002/rcs.331.

[7] T. Podder, J. Sherman, D. Clark, E. Messing, D. Rubens, J. Strang, L. Liao, R. Brasacchio, Y. Zhang, W. Ng, Y. Yu, Evaluation of Robotic Needle Insertion in Conjuction with in Vivo Manual Insertion in the Operating Room, IEEE, 2005, http://dx.doi.org/10.1109/ROMAN.2005.1513758.

[8] T.K. Podder, W.S. Ng, Y. Yu, Multi-channel robotic system for prostate brachytherapy, in: Conference Proceedings: …Annual International Conference of the IEEE Engineering in Medicine and Biology Society. IEEE Engineering in Medicine and Biology Society. Conference, 2007, pp. 1233–1236. http://dx.doi.org/10.1109/IEMBS.2007.4352520.

[9] E.M. Boctor, M.A. Choti, E.C. Burdette, R. Webster, Three-dimensional ultrasound-guided robotic needle placement: an experimental evaluation, International Journal (2008). http://dx.doi.org/10.1002/rcs.184.

[10] S.E. Salcudean, T.D. Prananta, W.J. Morris, I. Spadinger, A Robotic Needle Guide for Prostate Brachytherapy, Robotics and Automation, 2008. ICRA 2008. IEEE International Conference on, May 2008, pp. 2975–2981. http://dx.doi.org/10.1109/ROBOT.2008.4543662.

[11] N. Hata, R. Hashimoto, J. Tokuda, S. Morikawa, Needle guiding robot for MR-guided microwave thermotherapy of liver tumor using motorized remote-center-of-motion constraint, in: Proceedings of the 2005 IEEE International Conference on Robotics and Automation, pp. 1652–1656, April. http://dx.doi.org/10.1109/ROBOT.2005.1570350.

[12] G. Kronreif, M. Füurst, W. Ptacek, M. Kornfeld, J. Kettenbach, Robotic system for image guided therapie B-RobII, in: I. J. Rudas (Ed.), 15th International Workshop on Robotics in Alp-Adria-Danube Region, RADD 2006, Balantonfüred, Lake Balaton, Hungary.

[13] L.J. Puglisi, R.J. Saltaren, H.a. Moreno, P.F. Cárdenas, C. Garcia, R. Aracil Santonja, Dimensional synthesis of a spherical parallel manipulator based on the evaluation of global performance indexes, Robotics and Autonomous Systems 60 (8) (2012) 1037–1045. http://dx.doi.org/10.1016/j.robot.2012.05.013.

[14] M. Shoham, M. Burman, E. Zehavi, L. Joskowicz, E. Batkilin, Y. Kunicher, Bone-mounted miniature robot for surgical procedures: concept and clinical applications, IEEE Transactions on Robotics and Automation (5) (2003) 893–901. http://dx.doi.org/10.1109/TRA.2003.817075.

[15] T. Nakano, N. Sugita, T. Ueta, Y. Tamaki, M. Mitsuishi, A parallel robot to assist vitreoretinal surgery, International Journal of Computer Assisted Radiology and Surgery 4 (6) (2009) 517–526. http://dx.doi.org/10.1007/s11548-009-0374-2.

[16] C. Raoufi, A.A. Goldenberg, W. Kucharczyk, A new hydraulically/pneumatically actuated MR-compatible robot for MRI-guided neurosurgery, in: 2008 2nd International Conference on Bioinformatics and Biomedical Engineering, pp. 2232–2235. http://dx.doi.org/10.1109/ICBBE.2008.889.

[17] J. Li, S. Wang, X. Wang, C. He, Optimization of a novel mechanism for a minimally invasive surgery robot, The International Journal of Medical Robotics + Computer Assisted Surgery: MRCAS 6 (1) (2010) 83–90. http://dx.doi.org/10.1002/rcs.293.

[18] C. Gosselin, E. St Pierre, M. Gagne, On the development of the Agile Eye, IEEE Robotics & Automation Magazine 3 (4) (1996) 29–37. http://dx.doi.org/10.1109/100.556480.

[19] S.-H. Lee, W.-K. Kim, S.-M. Oh, B.-J. Yi, Kinematic analysis and implementation of a spherical 3-degree-of-freedom parallel mechanism, in: 2005 IEEE/RSJ International Conference on Intelligent Robots and Systems, IEEE, Singapore, 2005, pp. 972–977. http://dx.doi.org/10.1109/IROS.2005.1545080.

[20] R. Gregorio, Kinematics of the 3-UPU wrist, Mechanism and Machine Theory 38 (3) (2003) 253–263. http://dx.doi.org/10.1016/S0094-114X(02)00066-6.

[21] X. Kong, C. Gosselin, Type Synthesis of Parallel Mechanisms, in: Springer Tracts in Advanced Robotics, vol. 33, Springer, Berlin, Heidelberg, 2007, http://dx.doi.org/10.1007/978-3-540-71990-8.

[22] Y. Fang, L.-W. Tsai, Structure synthesis of a class of 3-DOF rotational parallel manipulators, IEEE Transactions on Robotics and Automation 20 (1) (2004) 117–121. http://dx.doi.org/10.1109/TRA.2003.819597.

[23] J.P. Merlet, Parallel Robots, second ed., Springer, The Netherlands, 2006.

[24] D. Zlatanov, R. Fenton, B. Benhabib, Singularity Analysis of Mechanisms and Robots via a Velocity-Equation Model of the Instantaneous Kinematics, vol. 2, IEEE Comput. Soc. Press, 1994, pp. 986–991. http://dx.doi.org/10.1109/ROBOT.1994.351325.

[25] L.W. Tsai, Robot Analysis: The Mechanics of Serial and Parallel Manipulators, John Wiley & Sons, Inc., 1999.

[26] K. Oen, L. Wang, Extreme reaches and maximal reachable workspace for rotary tools mounted on a Stewart platform manipulator, Journal of the Chinese Institute of Engineers 29 (6) (2006) 967–974.

[27] J.P. Merlet, D. Daney, Legs interference checking of parallel robots over a given workspace or trajectory, in: Robotics and Automation, IEEE, Orlando, Florida, 2006, pp. 757–762. http://dx.doi.org/10.1109/ROBOT.2006.1641801.

[28] R.J. Saltaren, J.M. Sabater, E. Yime, J.M. Azorin, R. Aracil, N. Garcia, Performance evaluation of spherical parallel platforms for humanoid robots, Robotica 25 (03) (2007) 257–267. http://dx.doi.org/10.1017/S0263574706003043.

[29] O. Ma, J. Angeles, Optimum Architecture Design of Platform Manipulators, Advanced Robotics, 1991. 'Robots in Unstructured Environments', 91 ICAR., Fifth International Conference on, vol. 2, June 1991, pp. 1130–1135. http://dx.doi.org/10.1109/ICAR.1991.240404.

Lisandro J. Puglisi received the B.S. degree in electronic engineering in 2006 from the Universidad Nacional de Tucumán, Argentina, and the M.S. degree in Automation and Robotics at the Universidad Politécnica de Madrid, Spain, in 2010. He is currently working toward the Ph.D. degree at the Center for Automation and Robotics of the UPM-CSIC, in Spain. His research interests include kinematics, dynamics and control of robotic parallel mechanisms and hydraulic robots applications.

Roque J. Saltaren received the degree in Mechanical Engineering from the Universidad del Valle, Cali, Colombia in 1980, the M.Sc. degree in Electrical Engineering from the Universidad de los Andes, Bogotá, Colombia in 1990, and the Ph.D. degree in Industrial Engineering from the Universidad Politécnica de Madrid, Madrid, Spain in 1996. He is currently Titular Professor at the Universidad Politécnica de Madrid, Spain. He is also Research Assistant of the Centre for Automation and Robotics of Universidad (UPM-CSIC). His research interests include parallel robots, robotics, and life science and robotics industrial applications. He has chaired several international conferences and workshops in robotics, and parallel robots.

Germán Rey Portolés received the Ph.D. degree in Physical Science from the Universidad de Valencia (1975). He has been director of the Radiophysics Unity at the Hospital Ramón y Cajal de Madrid (1978–1999). From 1999 onwards, he is the director of the Radiophysics Unity of Hospital Ruber Internacional. Since 2005, he is the director of the technical division of Hospital Ruber Internacional. He is the vice president of the Sociedad Española de Radiocirugía. He has been invited to many international congress and symposiums to give lecture on radiosurgery.

His main interests are focused toward minimally invasive surgery, particularly on the brain.

Hector Moreno received the B.S. degree in Mechanical Engineering in 2004 and the M.S. degree in Electrical Engineering in 2006, both from the Instituto Tecnologico de la Laguna, Mexico. He earned an M.S. degree in Automation and Robotics at the Universidad Politécnica de Madrid (UPM), Spain, in 2009. He is currently working toward the Ph.D. degree at the Center for Automation and Robotics of the UPM-CSIC, in Spain. His research interests include the kinematics, dynamics and control of robotic mechanical systems.

Pedro F. Cárdenas received the B.S. degree in Electronics from Universidad Pedagógica y Tecnológica de Colombia (UPTC) in 2000, and the M.S. degree in Industrial automation from the Universidad Nacional de Colombia (UNC), Bogotá in 2008. He is Assistant Professor at the Universidad Nacional de Colombia, Bogotá. He is currently working toward the Ph.D. degree in the Centre for Automation and Robotics of Universidad Politecnica de Madrid-CSIC, Spain. His research interests include the kinematics, dynamics control of robotic parallel mechanisms and surgery robotics.

Cecilia Garcia received the Ph.D. degree from Universidad Nacional de San Juan, Argentina in 2000. She is currently Assistant Professor at the Universidad Politécnica de Madrid, Spain. She is also Research Assistant of the Centre for Automation and Robotics of Universidad. Her research interests include telerobotics, artificial intelligence, robotics, and life science. She has chaired several international conferences and workshops in robotics, telerobotics, parallel mechanism, and multi-agent systems.